




Tumor Antigen-Tethered Spiked Virus-Like- Poly (Lactic-Co-Glycolic Acid)-Nanoparticle Vaccine Enhances Antitumor Ability Through Th9 Promotion in Mice

Ting-Wei Lin ¹, Po-Yu Chou ², Yen-Ting Shen², Ming-Thau Sheu ², Kuo-Hsiang Chuang^{3,4}, Shyr-Yi Lin^{5,6}, Chia-Yi Chang¹

¹Department of Veterinary Medicine, National Taiwan University, Taipei, Taiwan; ²School of Pharmacy, College of Pharmacy, Taipei Medical University, Taipei, Taiwan; ³PhD Program in Clinical Drug Development of Chinese Herbal Medicine, Taipei Medical University, Taipei, Taiwan; ⁴Graduate Institute of Pharmacognosy, Taipei Medical University, Taipei, Taiwan; ⁵Division of Gastroenterology and Hepatology, Department of Internal Medicine, Taipei Medical University Hospital, Taipei, Taiwan; ⁶Department of General Medicine, School of Medicine, College of Medicine, Taipei Medical University, Taipei, Taiwan

Correspondence: Shyr-Yi Lin; Chia-Yi Chang, Email sylin@tmu.edu.tw; chiayichang@ntu.edu.tw

Purpose: Immunotherapy emerges as a promising frontier in cancer therapy and prevention. This study investigates the capacity of tumor-antigenic nanoparticles, specifically ovalbumin-tethered spiked virus-like poly(lactic-co-glycolic acid) nanoparticles (OVA-sVLNP), to effectively elicit humoral and cellular immune responses against tumors.

Methods: OVA-sVLNP were synthesized through thiol-maleimide crosslinking using a single emulsion method. Comprehensive characterization was performed through Nuclear Magnetic Resonance (NMR), dynamic light scattering, Cryo-electron microscopy (Cryo-EM), confocal microscopy, and flow cytometry. Immunogenicity was evaluated using an enzyme-linked immunosorbent assay (ELISA) for quantifying immunoglobulin levels (IgG, IgG1, IgG2a) and cytokines in mouse sera. Flow cytometry profiled cellular immune responses in mouse spleens, and organ biosafety was assessed using immunohistochemistry and hematoxylin and eosin (H&E) staining.

Results: OVA-sVLNP had a mean particle size of 193.8 ± 11.9 nm, polydispersity index of 0.307 ± 0.04 , and zeta potential of -39.6 ± 10.16 mV, remaining stable for one month at 4°C. In vitro studies revealed significant upregulation of CD80/CD86 in dendritic cells, indicating robust activation. In vivo, the optimal concentration (V25) induced potent IgG, IgG1, and IgG2a antibodies, significant populations of CD3⁺CD4⁺, CD3⁺CD8⁺, and a rare subset of CD3⁺CD4⁺CD8⁺ memory T cells. Notably, Th9 induction resulted in the secretion of IL-9, IL-10, and other cytokines, which are crucial for orchestrating cytotoxic T cell activity and antitumor effects. Overall, higher doses did not improve outcomes, highlighting the significance of optimal dosing.

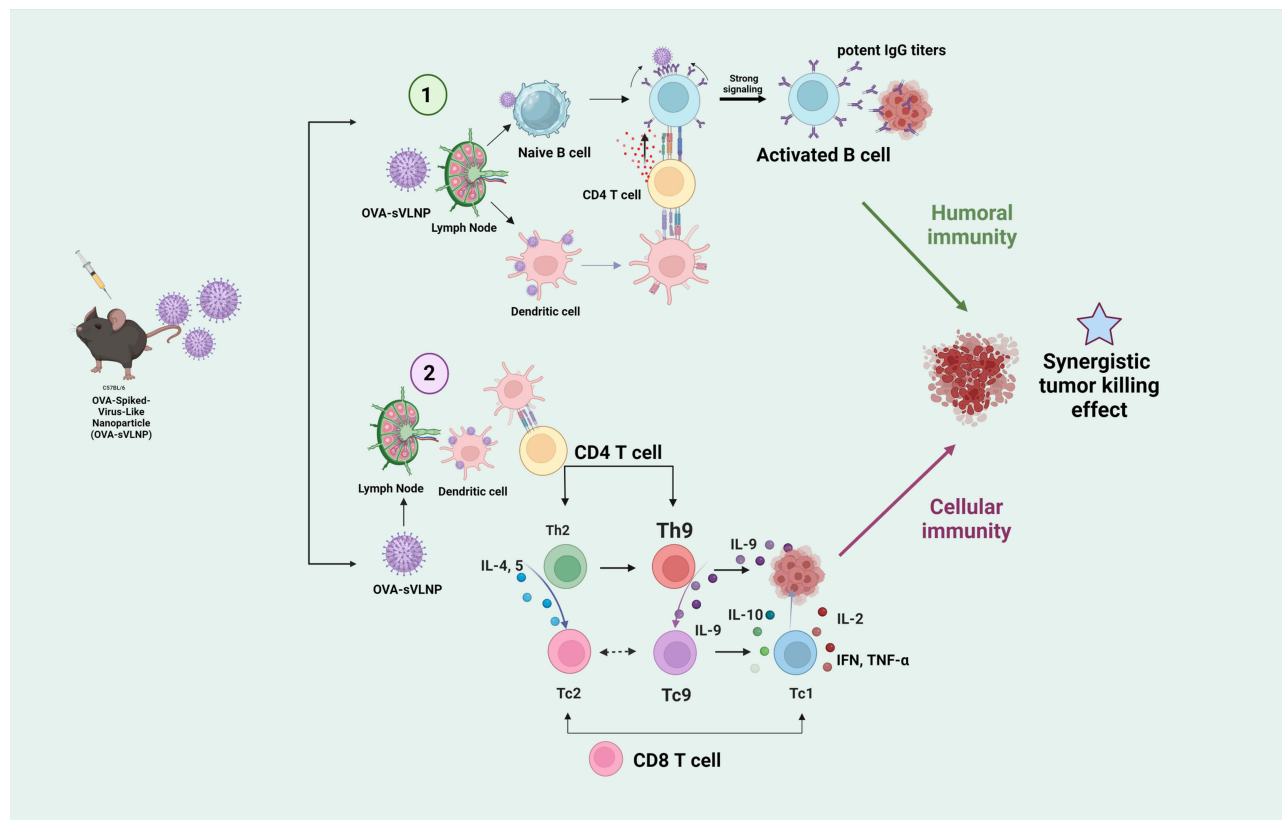
Conclusion: This study demonstrated potent immunogenicity of OVA-sVLNP, characterized by the induction of specific IgG antibodies and the stimulation of cellular immune responses, particularly tumor-killing Th9 cells. The simplicity and cost-effectiveness of the manufacturing process augment the potential of OVA-sVLNP as a viable candidate for antitumor vaccines, opening new avenues for cancer prevention and cell-based therapeutic strategies.

Keywords: tumor antigen-spiked virus-like nanoparticles, PLGA nanoparticles, cancer vaccine, ovalbumin, T helper 9, antitumor

Introduction

Cancer vaccines have been demonstrated to have considerable potential.^{1,2} Over the past four decades, these vaccines have primarily worked by activating the immune systems of patients to prevent and target tumors, employing either cellular or humoral immune responses. Clinical trials or preclinical studies have focused on the interaction of tumor antigens or biomarkers with adjuvants or other costimulatory factors.³⁻⁶ The delivery system is a critical component of these vaccines and is responsible for delivering tumor antigens and activators to the immune system. One of the most

Graphical Abstract



successful delivery vehicles utilizes virus-like nanoparticles (VLNPs), which have attracted considerable attention for its use against various cancers.^{7–13}

VLNPs typically range from 20 to 200 nm in diameter and resemble many viruses in size.¹⁴ They effectively mimic virus entry into host cells without causing viral infection, utilizing their complex, multimeric, or self-assembling structures. VLNPs are classified as enveloped or non-enveloped, depending on whether a lipid envelope is present.¹⁵ The efficacy of these vaccines depends on their ability to induce a range of immune responses. These responses can occur independently or synergistically, involving key immune cells such as antigen-presenting cells (APCs), helper and cytotoxic T cells, natural killer (NK) cells, and tumor-resident myeloid cells.

A review study published in 2012¹⁶ reported that activated T helper cells can differentiate into either effector T helper 1 (Th1) or T helper 2 (Th2) cells. These two subsets of effector CD4⁺ T cells are defined by the specific cytokines they secrete and their distinct immune functions. Interleukin 9 (IL-9) is a cytokine originally associated with the Th2 phenotype and plays a vital role in allergic mechanisms, resistance to parasites, and antitumor immunity.^{17,18} In 2008, T helper 9 (Th9) cells were identified as a new subset of CD4⁺ T cells, notable for their simultaneous production of Interleukin 9 and Interleukin 10 (IL-10), distinguishing them from Th2 cells.¹⁹

A study investigating the effects of IL-9 neutralization in a B16 melanoma lung model, noted for its low immunogenicity, also introduced tumor-specific Th9 cells in both prophylactic and therapeutic tumor models. The findings suggest that IL-9 and Th9 cells provide protection against tumor development.¹⁸ Interestingly, Th9 cells have been observed to recruit dendritic cells to tumor sites, promoting antigen presentation in tumor-draining lymph nodes (TDLNs).²⁰ IL-9 serves dual roles in tumor suppression: it not only directly triggers apoptosis in malignant cells, but also stimulates the initiation of both innate and adaptive antitumor immune responses. Moreover, the study highlighted

that ectopic expression of membrane-bound IL-9 (MBIL-9) can induce cytotoxic effects in T helper cells, specifically targeting CT26 tumor cells. Additionally, MBIL-9 also amplifies the cytolytic potential of CD4⁺ and CD8⁺ T lymphocytes.²¹ Furthermore, the study identified a rare population of activated CD4⁺CD8⁺ double-positive T cells in mouse spleens, further underscoring IL-9's pivotal role in augmenting the activation of cytotoxic T cells.

Previous research has increasingly focused on the use of small protein antigens processed by APCs, especially dendritic cells (DCs). Mature DCs migrate to lymph nodes (LNs), a process that is essential for activating antitumor T cells, including CD4⁺ (helper) T cells, and CD8⁺ (cytotoxic) T cells. This pivotal function renders DCs primary targets in developing protein antigen-based vaccines, such as ovalbumin (OVA).^{22–24} The monomeric structure of OVA, consisting of a 44.5 kDa molecular weight and a sequence of 385 amino acids, exhibits dual gene polymorphism and four unbound sulfhydryl groups, enhancing its resilience against tumor relapse.²⁵ However, challenges such as immunogenicity, intracellular delivery, protection against enzymatic degradation, efficient uptake by DCs, and prolonged circulation time. These challenges underscore the necessity for nanoparticle-based strategies to overcome these limitations in utilizing OVA.^{23,25}

Poly(lactic-co-glycolic acid) (PLGA) is an effective biodegradable polymer, valued primarily for its degradation into lactic acid and glycolic acid²⁶—both endogenous metabolites that the body easily processes via the Krebs cycle. This characteristic renders PLGA particularly suitable for drug delivery and biomaterial applications due to its minimal systemic toxicity.²⁷ The use of Poly(D, L-lactide-co-glycolide) (PLGA) in designing particulate antigen delivery systems, specifically for cancer vaccines and antitumor therapy, has been extensively researched. The improved efficacy of vaccines employing PLGA particles is attributed to their capacity to consistently release antigens, thereby enabling the precise targeting of APCs, specifically dendritic cells (DCs). Such targeting is crucial for inducing cytotoxic T cell immunity.²⁸ Furthermore, it is crucial to modify the surface of PLGA particles, by adding hydrophilic moieties such as polyethylene glycol (PEG) polymers. These modifications are designed to interact with surface receptors on dendritic cells, enhancing selective binding affinity to dendritic cellular targets, promoting receptor-mediated endocytosis, and subsequently increasing antigen-presenting efficiency to various helper T cells, such as the CD4⁺ subsets Th1, Th2, Th9, and Th17 cells.^{28,29}

This study outlines the process of combining the advantages of Ovalbumin (OVA) and VLNP to create highly effective antigen bindings. This is achieved by tethering OVA protein antigens to maleimide-PEG-PLGA nanoparticles (MAL-VLNP) through the thiol-maleimide click reaction, resulting in the creation of OVA-spiked virus-like PLGA nanoparticles (OVA-sVLNP). The specific aim is to target dendritic cells using OVA-sVLNP, leveraging their capabilities to generate robust humoral and cellular immune responses for efficient tumor cell elimination. OVA serves as the model protein, representing tumor-associated proteins. The OVA-sVLNP formulation has demonstrated noteworthy enhancement in both B cell and T cell immune responses following vaccination in mouse models. This finding serves as a predictive indicator of the potential antitumor efficacy of the OVA-sVLNP formulation. This innovative approach offers a promising platform for the development of therapeutic cancer vaccines.

Materials and Methods

Materials

This study used Poly(D,L-lactide-co-glycolide) (RESOMER, RG 502, PLGA) from Evonik (Essen, Germany); DSPE-PEG020-Maleimide from Biopharma PEG (Watertown, MA, USA); Soybean lecithin (Lipoid S-100) from Sigma-Aldrich (Ludwigshafen, Germany); and Ovalbumin (extracted from chicken egg whites) from Sigma-Aldrich, (St. Louis, MO, USA). The Amicon Ultra-15 Centrifugal Filter Units (Merck, 100 kDa) and the DC2.4 (SCC142) murine bone marrow-derived dendritic cell line were purchased from Merck KGaA (Darmstadt, Germany). RPMI 1640 medium, nonessential amino acids, L-glutamine, 2-β-mercaptoethanol, 4-(2-hydroxyethyl)-1-piperazineethanesulfonic acid (HEPES), Hoechst 33342, LysoTracker Red DND-99, and NHS-Fluorescein CBQCA Protein Quantitation Kit were purchased from Thermo Fisher Scientific (Waltham, MA, USA). DiI iodide (1,1-dioctadecyl-3,3,3,3-tetramethylindotricarbocyanine iodide) was obtained from ATT Bioquest (Pleasanton, CA, USA). C57BL/6 mice and their purified dye-free diets were purchased from BioLASCO Taiwan (Taipei, Taiwan). PE anti-mouse CD80 Antibody, APC anti-mouse CD86 Antibody, APC anti-mouse MHCII Antibody, APC anti-mouse CD3 Antibody, Percp/cy5.5 anti-mouse CD4 Antibody, and PE anti-mouse CD8a Antibody

were obtained from BioLegend (San Diego, CA, USA). Goat Anti-Mouse IgG1-HRP and Goat Anti-Mouse IgG2a HRP were received from Southern Biotech (Birmingham, Alabama, USA). Anti-ovalbumin IgG (mouse) enzyme-linked immunosorbent assay (ELISA) Kit, Anti-ovalbumin IgG1 (mouse) ELISA Kit, and Anti-ovalbumin IgG2a (mouse) ELISA Kit were obtained from Cayman Chemical (Ann Arbor, MI, USA). TMB Substrate was purchased from Clinical Science (Mansfield, MA, USA). Dulbecco's modified Eagle medium, Heat-inactivated fetal bovine serum (FBS), Penicillin-Streptomycin Amphotericin B solution (10,000 units/mL Penicillin G sodium salt, 10 mg/mL Streptomycin sulfate, 25 µg/mL Amphotericin B with 8.5 g/L NaCl), and trypsin-EDTA (0.25% trypsin / 2.21 mm EDTA in HBSS without sodium bicarbonate, calcium, or magnesium) were obtained from Corning (Corning, NY, USA).

Preparation and Characterization of Ovalbumin-Spiked Virus-Like PLGA Nanoparticles (OVA-sVLNP) Using a Maleimide Linker on MAL-PEG VLNP

In this study, the preparation of ovalbumin-spiked virus-like PLGA nanoparticles (OVA-sVLNP) involved a modified single ultrasonic shaking emulsion phase method, adapted from another study.³⁰ Initially, the inner phase polymer solution was created by dissolving PLGA in dichloromethane. Concurrently, the external aqueous solution was prepared using lecithin with DSPE-PEG2000-Maleimide in 0.001 M phosphate buffer at pH 5. When the internal phase was injected into the external phase, the mixture was subjected to ultrasonic probe sonication (Q700, Q Sonica LLC, USA) at a frequency of 7% amplitude for 1 s, with 2-s intervals over a 2-min emulsification period. Following this, the oil and water monophasic nanoparticle solution was transferred to a 40°C circulating water bath and a chemical exhaust cabinet to allow solvent volatilization at 500 rpm for 1 h. Finally, the solution was centrifuged using a 100-kDa molecular weight Amicon filter tube at $500 \times g$ and 25°C for 30 min to obtain maleimide PEG-inserted virus-like PLGA nanoparticles (MAL-VLNP). The next step involved mixing an appropriate volume of MAL-VLNP with the ovalbumin (OVA) reaction solution, where OVA was dissolved in 0.001 M phosphate buffer at pH 7. This solution underwent a thiol-maleimide crosslinking reaction between the thiol group on OVA and the maleimide group on MAL-VLNP at room temperature. The reaction was achieved by rotating the mixture at 500 rpm for 4 h. The nanoparticles were then concentrated using an Amicon filter tube with a 100 kDa molecular weight cutoff, involving centrifugation at $500 \times g$ and 25°C for 30 min and subsequent rinsing with deionized water. To remove free substances, the solution was centrifuged again at $500 \times g$ and 25°C for 5 min, followed by three rounds of rinsing with deionized water. Finally, the OVA-sVLNP was obtained by freeze-drying the resultant product.

The content of the maleimide group in MAL-VLNP (dissolved in a chloroform-d solvent) was determined by identifying the chemical shift peak at $\delta = 6.7$ ppm for the maleimide functional group using a 600 MHz nuclear magnetic resonance instrument (Agilent 600 MHz DD2 nuclear magnetic resonance [NMR]). The particle size, polydispersity index (PDI), and interface potential (Zeta potential) of OVA-sVLNP and MAL-VLNP were analyzed using a nanoparticle size potential distribution analyzer (DKSH & Malvern Zetasizer Nano ZSP). Each measurement was repeated three times for each group, and the mean and standard deviation (SD) were calculated using Prism 8.3 software to ensure experimental reproducibility. The physicochemical stability of ovalbumin-spiked virus-like-PLGA nanoparticles (OVA-sVLNP) was verified at 4°C. This involved monitoring changes in particle size and zeta potential using the nanoparticle size potential distribution analyzer (DKSH & Malvern Zetasizer Nano ZSP) at predetermined intervals (days 1, 7, 14, 21, and 28).

For quantifying the OVA content in the OVA-sVLNP, the nanoparticles were suspended in a 0.1 M boric acid solution adjusted to pH 8. The CBQCA Protein Quantitation Kit was used for quantification, and the concentration was detected using an ELISA reader (BioTek Instruments, USA) at 550nm. The morphology of the OVA-sVLNP was analyzed using Cryo-electron microscopy (Cryo-EM).

Cell Culture

Murine dendritic cells (DC2.4) were cultured in RPMI-1640 (Sigma Cat. No. R0883) supplemented with 10% FBS (Cat. No. ES-009-B), 1X L-Glutamine (Cat. No. TMS-002-C), 1X nonessential amino acids (Cat. No. TMS-001-C), 1X

HEPES Buffer Solution (Cat. No. TMS-003-C), and 0.0054X β -Mercaptoethanol (Cat. No. ES-007-E). The DC2.4 cells were trypsinized using trypsin-EDTA and maintained in a humidified incubator with 5% CO₂ at 37°C.

In vitro Cellular Uptake Assay

The murine dendritic cells (DC2.4) were seeded in six-well cell culture plates and incubated overnight. Subsequently, 1 mL of solution containing Control (culture medium), Bare (sVLNP), V10 (OVA-sVLNP, OVA = 10 μ g/mL), V25 (OVA-sVLNP, OVA = 25 μ g/mL), V50 (OVA-sVLNP, OVA = 50 μ g/mL), and V100 (OVA-sVLNP, OVA = 100 μ g/mL) nanoparticles were added to the respective wells. These were incubated at 37°C with 5% CO₂ for 24 h. Following the 24-h culture period, the supernatant was removed, and the cells were rinsed twice with 1 \times phosphate-buffered saline (PBS). Subsequently, 0.2 mL of 0.1% trypsin-EDTA (Corning) was added for cell resuspension, and the cells were washed again with 1x PBS. Two different cell-marker fluorescently labeled antibodies, APC anti-mouse CD86 antibody (BioLegend) and PE anti-mouse CD80 antibody (BioLegend), were used to stain the cells for 20 min on ice. The cell pellets were washed and resuspended with 1 \times PBS and then analyzed using flow cytometry (SA3800) to observe the maturation ability of DC2.4.

To synthesize FITC-conjugated OVA-sVLNP, a 10 mg/mL NHS-FITC solution, dissolved in dimethyl sulfoxide (DMSO), was used. Prepared OVA-sVLNP was suspended in a 50 mM boric acid buffer at pH 8.5. The reaction, maintaining a 1:15 molar ratio of OVA to NHS-FITC, proceeded at room temperature for 1 h in a light-protected environment. Concentration of the nanoparticles was achieved using an Amicon filter tube with a 100 kDa molecular weight cutoff, followed by centrifugation at 500 \times g for 10 min and three sequential rinses with deionized water.

The DC2.4 murine dendritic cells were cultured overnight on a 35 mm glass bottom dish (Ibidi). Subsequently, FITC-OVA-sVLNP was administered at distinct time intervals of 6, 12, 24, and 36 h. LysoTracker at a concentration of 50 nM was introduced into the culture medium for 45 min, followed by three rinses with fresh culture medium. Post-rinsing, Hoechst at a concentration of 2 μ g/mL was added to the culture medium for 30 s, followed by three washes with new culture medium. The assessment of cellular phagocytosis dynamics over various time points was conducted utilizing a state-of-the-art super-resolution white light-linked focus real-time imaging platform (Stellaris 8 confocal microscope).

In a separate experiment, DC2.4 murine dendritic cells were cultured in a 12-well culture plate overnight. At specific intervals of 6, 12, 24, and 36 h, distinct dosages of FITC-OVA-sVLNP were administered. Cells were then resuspended using 0.1% trypsin-EDTA (Corning) and analyzed using flow cytometry (SA3800) to assess the phagocytic activity of DC2.4 cells.

In vivo Biodistribution

The lipophilic near-infrared photostain DiR iodide was selected for its excitation wavelength of 748 nm and emission wavelength of 780 nm. This stain was utilized to encapsulate within OVA-sVLNP to form DiR-encapsulated OVA-sVLNP. The purpose of this encapsulation was to aid in biodistribution analysis by leveraging the lipophilicity and near-infrared properties of DiR iodide for tracking the nanoparticles.

Before administering the drug, C57BL/6 mice were fed a dye-free purified diet for 2–3 days. This dietary measure was to eliminate potential interference between the general feed and the fluorescence of DiR. Each group of animals received an intramuscular injection of 20 μ L of DiR-encapsulated OVA-sVLNP. The in vivo migration of OVA-sVLNP was observed using the IVIS Lumina III XRMS in vivo imaging system (PerkinElmer, UK) at specific time points: 2, 6, 24, 48, 72, and 168 h post-administration. The accumulation pattern of DiR-encapsulated OVA-sVLNP in the ipsilateral lymph nodes was determined by capturing DiR fluorescence signals with the IVIS system.

Mouse Immunization and Humoral Immunity Assessments

The C57BL/6 mice were stratified randomly into five groups, with each group comprising four mice (n = 4). The mice received an intramuscular injection of 20 μ L OVA-sVLNP at 2-week intervals, totaling three injections. On days 7, 21, 35, 63, and 84 after the initial injection (denoted D7, D21, D35, D63, and D84, respectively), approximately 300 μ L of whole blood was extracted from the cheek of each mouse using a 26G needle. These samples were centrifuged at 4000 rpm for 10 min at 4°C to separate the serum, which was subsequently preserved at -80°C for subsequent analyses.

To assess immunoglobulin G titers, an ELISA protocol was employed. Initially, each well of a 96-well plate was coated with 100 μ L of ovalbumin solution and incubated overnight at 4°C. The wells were then rinsed three times with 250 μ L of rinse solution. Subsequently, 100 μ L of blocking solution was added to each well and incubated at 150 rpm and 25°C for 1 h, followed by three more rinses. Subsequently, 100 μ L per well of standard curve solutions and serum samples (diluted from 1:500 to 1:5000) were added and incubated for 2 h at 150 rpm and 25°C. After another set of three rinses, 100 μ L per well of the secondary antibody, Goat Anti-Mouse IgG HRP detection antibody (diluted at 1:10,000), was introduced and incubated for 1 h at 150 rpm and 25°C. Following three rinses, 100 μ L per well of TMB solution was added and incubated for 10 min at 150 rpm and 25°C. The reaction was terminated by introducing 50 μ L per well of 2N sulfuric acid solution, and the absorbance was measured at a visible light wavelength of 450 nm (ThermoScientific, VARIOSKAN LUX).

For detecting immunoglobulin G1 (IgG1), the methodology mirrored that used for immunoglobulin G (IgG) titer measurement, with nuanced adjustments. Specifically, serum samples for D7 were diluted at a ratio of 1:500, and samples from D21, D35, D63, and D84 were diluted at a ratio of 1:5000. The secondary antibody, Goat Anti-Mouse IgG1 HRP detection antibody was diluted at 1:40000, aligning with the standardized ELISA protocols utilized in IgG titer determination.

The methodology employed in detecting immunoglobulin G2a (IgG2a) closely parallels the established procedure for assessing immunoglobulin G (IgG) titers, albeit with distinct variations. Specifically, serum samples from D7 were diluted at 1:50, and samples from D21, D35, D63, and D84 were diluted at 1:100. The secondary antibody, Goat Anti-Mouse IgG2a HRP detection antibody, was diluted at 1:8000, aligning precisely with the standardized ELISA protocols utilized in determining IgG titers.

Evaluation of T Cell-Derived Multiple Cytokines

The BioLegend multi-analyte flow assay kit was used to assess the cytokine profiles of distinct T cell populations in mouse serum. This involved processing mouse serum samples (D0, D7, D21, D35, D63, D84) and standard calibration samples using a 96-well assay filter plate. The protocol was conducted with meticulous care, starting with the thawing of samples on ice. Initially, the filter plate was washed with 100 μ L of 1 \times wash buffer, which was subsequently aspirated. Subsequently, 25 μ L of matrix buffer, assay buffer, and test serum were sequentially added to each well, followed by the addition of 25 μ L of capture beads. This mixture was then agitated at room temperature for 2 h at 500 rpm. After this incubation, the plate underwent two washes with 1 \times wash buffer and the buffer was aspirated. A 25 μ L volume of detection antibody was added, followed by an incubation at room temperature for 1 h at 500 rpm. Subsequently, 25 μ L of SA-PE was introduced into the assay and incubated at room temperature for 30 min at 500 rpm. After two more washes with 1 \times wash buffer and aspiration of the buffer, the beads were reconstituted in 150 μ L of 1 \times wash buffer. The final step involved flow cytometry analysis using BD Celesta for data acquisition, with post-acquisition data analysis conducted utilizing the LEGENDplex Data Analysis software.

Evaluation of the Proportion of B and T Cells from Mouse Splenocytes

On the 84th day after the initial injection, the spleens of euthanized mice were harvested and sectioned into small fragments in a 6 cm cell culture dish. After sectioning, 5 mL of a solution containing 1 mg/mL Collagenase D and 100 μ g/mL DNase I were added, initiating a 30-min incubation period at 37°C with 5% CO₂ in a cell culture incubator. The resultant cell suspension was then filtered through a 40 μ m nylon cell strainer, followed by a 5 mL wash using 1 \times PBS to collect the filtrate. The filtrate underwent centrifugation at 300 \times g for 7 min, after which the supernatant was discarded. Subsequently, the cell pellet was treated with 1 mL of 1 \times red blood cell lysis buffer (RBC lysis buffer, BD) for 1-min, followed by two washes with 1 \times PBS and a final centrifugation at 300 \times g to isolate the spleen cells. To isolate T cells, fluorescently labeled anti-mouse antibodies (CD3-APC, CD4-Percp/cy5.5, and CD8a-PE sourced from BioLegend) were individually introduced to the splenocytes in flow tubes, allowing for a 30-min staining period in the dark. Similarly, B cells were isolated using different fluorescent anti-mouse antibodies (CD45R/B220-Percp/cy5.5 and MHCII-APC sourced from BioLegend), each introduced separately to the flow tubes containing the splenocytes and

stained for 30-min in the dark. After staining, the supernatant was removed, and the cells were rinsed twice with $1\times$ PBS. Finally, the cells were suspended for subsequent analysis utilizing flow cytometry techniques.

Assessment of Chemokine Function from Mouse Lymph Nodes

Simultaneously, on the eighty-fourth day after the initial inoculation, the bilateral groin lymph nodes were harvested from euthanized mice. These lymph nodes were first fixed by immersing them in a 10% formalin solution for 72 h, and then preserved by storing in PBS at 4°C. For immunohistochemistry (IHC) staining assays, the lymph node tissues were treated with anti-mouse CXCL3 or CXCL13 antibodies (BioLegend). The tissue sections were then analyzed by Toshon Technology. These immunohistochemical stains were graded on a semiquantitative scale according to the positive staining ratio within the lymph nodes.³¹

Biosafety Assessments

On day 84, after the initial injection, the mice were euthanized for the retrieval of vital organs, including hearts, livers, lungs, kidneys and lymph nodes. These organs were immersed in a 10% formalin solution for fixation. The organ specimens then underwent a series of processing steps conducted by Toshon Technology. These steps included paraffin embedding, tissue sectioning, and histological staining using hematoxylin and eosin (H&E). The stained tissues were observed under a microscope with panoramic scanning capabilities in visible light to assess any histopathological changes. Throughout the experimental period, the body weight of the C57BL/6 mice was monitored weekly. This regular monitoring continued up to the 12th week, at which point the mice were euthanized.

Statistics

GraphPad Prism software (V8.3, GraphPad Software, San Diego, CA, USA) was used for data analysis. All data are expressed as the mean \pm SD. Statistical significance was evaluated using either a one-way analysis of variance (ANOVA) or two-way ANOVA, followed by Tukey's multiple-comparisons test for assessing differences between multiple groups. A *p* value of <0.05 indicated statistical significance.

Results

Characterization and Optimization of OVA-sVLNP Formulation

The assembly methods used to prepare OVA-sVLNP are depicted in [Figure 1A](#). The process involved varying the proportions of DSPE-PEG2000-Mal and ovalbumin to create distinct formulations with various amounts of DSPE-PEG2000-MAL insertion on the surface of PLGA nanoparticles spiked with OVA, as detailed in [Table 1S](#). The optimal formulations, denoted as L-OVA-sVLNP, M-OVA-sVLNP, and H-OVA-sVLNP, were derived from specific ratios of DSPE-PEG2000-Mal at 0.798, 1.261, and 1.766 mg, respectively, each maintaining a DSPE-PEG2000-Mal: OVA molarity ratio of 1:1. Notably, the particle sizes across these optimized groups consistently remained approximately 200 nm ([Table 2S](#) and [3S](#)). This uniformity underscores a consistent and optimal distribution for each formulation.

The OVA-sVLNP formulations (L-OVA-sVLNP, M-OVA-sVLNP, and H-OVA-sVLNP) had particle sizes that ranged from approximately 150 to 200 nm, with a PDI of approximately 0.3 ([Figure 1B](#)). This size profile is advantageous because it promotes phagocytosis by peripheral dendritic cells and ensures efficient lymphatic drainage. Studies have indicated that particle zeta potential values exceeding +25 mV or falling below -25 mV reduce particle aggregation and confer a high degree of stability.³² This study found that the zeta potential for each OVA-sVLNP group consistently ranged between -30 and -40 mV ([Figure 1C](#)), indicating a robust level of stability for all particle formulations. The optimized H-OVA-sVLNP of Dynamic Light Scattering (DLS) graph is shown in [Figure 1D](#), and the morphology of OVA-sVLNP is depicted in [Figure 1E](#) at a lower magnification using Cryo-EM, which exhibited the consistent result with DLS findings. A more detailed examination ([Figure 1F](#)) revealed finely textured particles on the surface of sVLNP particles, indicative of OVA binding to the sVLNP surface.

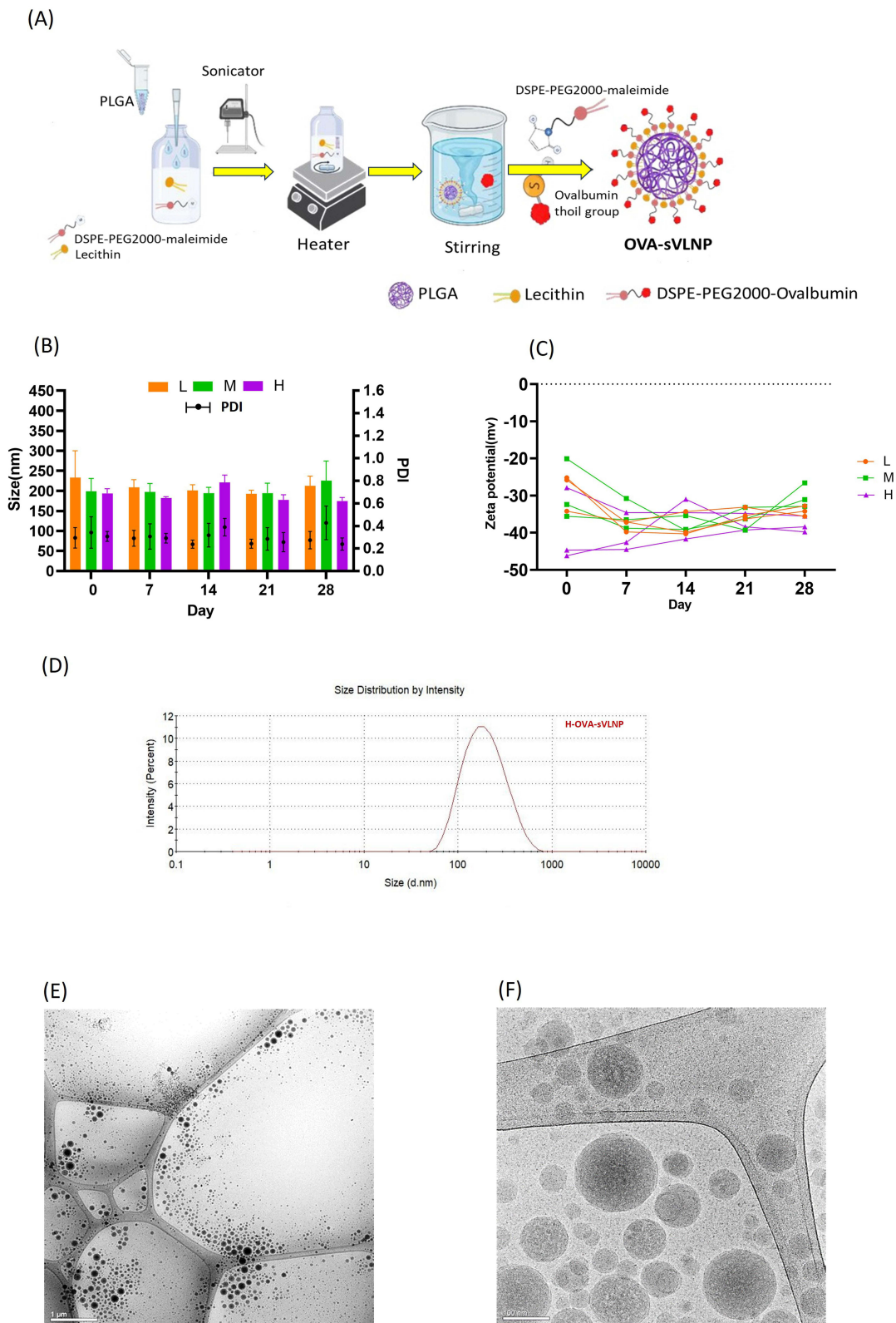


Figure 1 Physical characterization of OVA-sVLNP. **(A)** Schematic diagram of the OVA-sVLNP preparation process. **(B)** Particle size and polydispersity index (PDI), and **(C)** zeta potential of L-, M-, and H-OVA-sVLNP were monitored over a period of 1 month. **(D)** Dynamic light scattering (DLS) analysis of H-OVA-sVLNP. **(E)** Lower magnification Cryo-EM image of H-OVA-sVLNP (scale bar: 1 μ m). **(F)** High magnification Cryo-EM image showing detailed surface texture of H-OVA-sVLNP (scale bar: 100 nm). L: L-OVA-sVLNP (low OVA loading ratio), M: M-OVA-sVLNP (medium OVA loading ratio), and H: H-OVA-sVLNP (high OVA loading ratio).

Analysis of Maleimide Functional Group by NMR

The study solubilized DSPE-PEG2000-Maleimide in DMSO to create a range of standard solutions with concentrations from 0.3125 to 10 mg/mL. This process is illustrated in Figure 2A. The chemical shift peak at $\delta = 6.7$ ppm for the maleimide functional group was identified using a 600 MHz NMR spectrometer and subsequently quantified through integration. The resulting calibration curve, depicted in Figure 2B, indicated a linear correlation between the integrated area and concentration, following the equation $y = 0.0107x + 0.0012$ with an R^2 value of 0.998. This consistency affirmed the reliability of concentration measurements within this specified range on a daily basis. Similarly, Figure 2C depicted a consistent linear trend for same-day confirmations, as represented by the equation $y = 0.0107x + 0.0011$ with an R^2 value of 0.998. This consistency affirmed the reliability of concentration measurements within this specified concentration range on a daily basis.

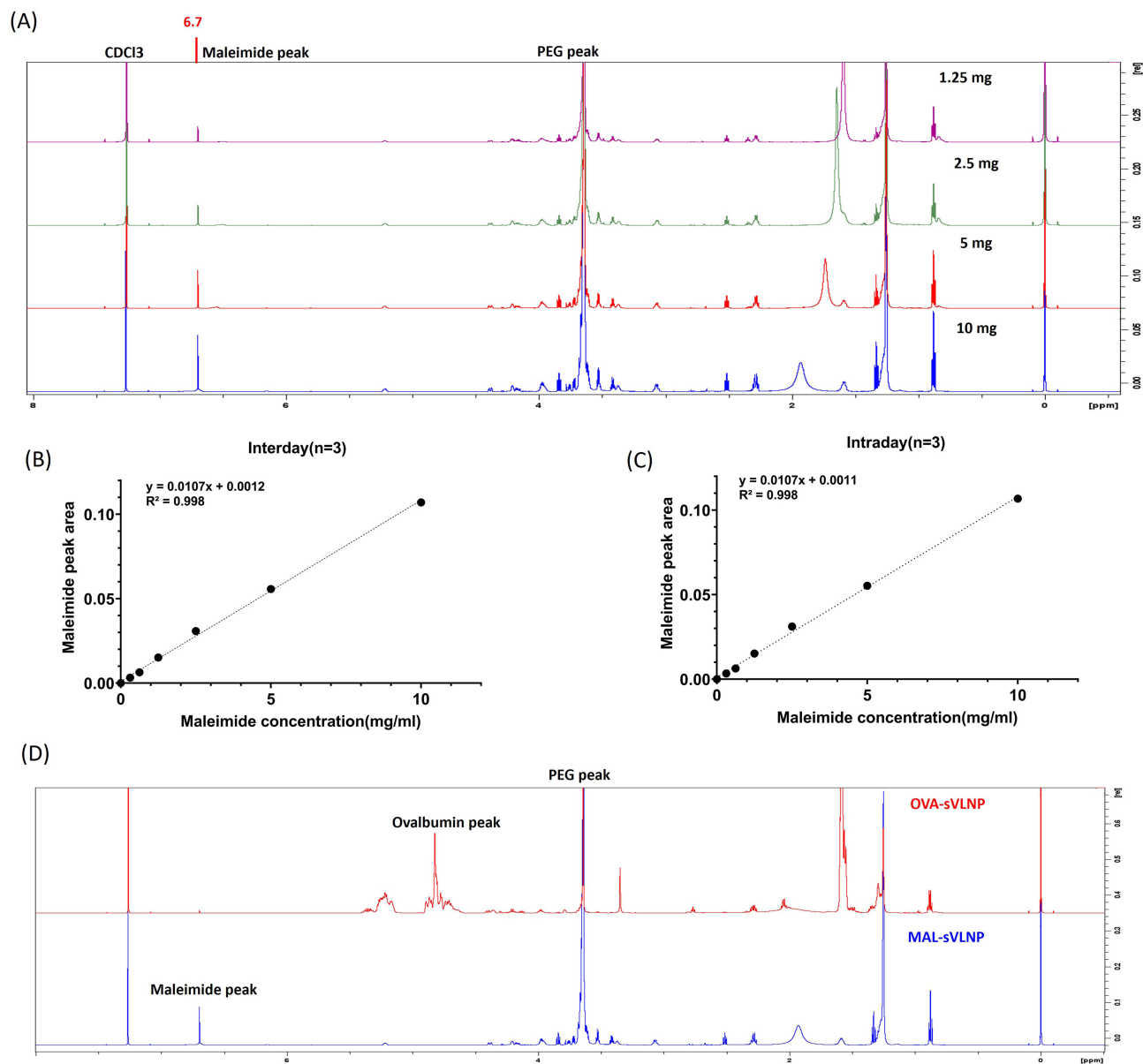


Figure 2 NMR analysis of maleimide functional group. **(A)** Proton H spectrum of DSPE-PEG2000-maleimide across a concentration range of 0.3125 to 10 mg/mL with precise detection of the maleimide functional group peak using a 600 MHz NMR spectrometer. **(B)** Interday standard curves of DSPE-PEG2000-maleimide. **(C)** Intraday standard curves of DSPE-PEG2000-maleimide. **(D)** NMR spectrum displaying the successful conjugation of OVA in OVA-sVLNP via thiol-maleimide reaction. (1,2-distearoyl-sn-glycero-3-phosphoethanolamine, DSPE; polyethylene glycol, PEG).

In analyzing the NMR spectrum of OVA-sVLNP, a notable change was observed: the interaction between maleimide and OVA resulted in a bonding event, as evidenced by the emergence of an OVA-associated peak. Notably, a shift in the maleimide peak appeared, indicative of crosslinking interactions, which obscured the original maleimide peak. This observation is illustrated in Figure 2D.

Based on these physical characteristics, the H-OVAL-sVLNP formulation was selected as the most optimal for comparing the effects of varying antigen concentrations of OVA (0, 10, 25, 50, and 100 mg/mL designated as V10, V25, V50, and V100, respectively) on immunological responses in subsequent studies.

Evaluation of the Activation and Phagocytosis Efficacy of OVA-sVLNP

The study focused on how the immune system responds to the introduction of foreign antigens, particularly examining the role of dendritic cells. When immature dendritic cells encounter antigens, they migrate towards inflammatory tissues, engulf the antigen through phagocytosis, and gradually mature. This maturation involves the upregulation of surface cell markers CD80 and CD86, which are pivotal for activating T cells.³³ The data revealed that the expression levels of CD80 and CD86 in each OVA-sVLNP group were significantly higher than in the Bare group (Figure 3A). Particularly notable was the augmented expression of these markers in the V25 group, which significantly differed with those of the Bare group ($***p < 0.001$, $****p < 0.0001$) but not the OVA-sVLNP groups. The study also investigated the phagocytosis of OVA-sVLNP by dendritic cells at various time points (6, 12, 24, and 36 h) using flow cytometry analysis (Figure 3B). A rapid saturation in uptake was observed within approximately 6 h. Additionally, a direct correlation emerged between OVA concentration and cellular engulfment, indicating increased uptake with elevated OVA concentrations. Statistical analysis revealed significant differences between each OVA-sVLNP group and the Bare group. Furthermore, the OVA-sVLNP groups differed in various respects, underscoring the nuance in differences between the effects of each concentration. ($****p < 0.0001$)

Following 12 h of co-culture with dendritic cells, OVA-sVLNP was observed to be phagocytosed by dendritic cells and localized within lysosomes (Figure 4A). A significant transition was observed at 36 h, with portions of OVA-sVLNP beginning to depart from the lysosomal compartments and translocate towards the nucleus. This phenomenon is observable in the confocal microscopy images, where the lysosome tracker is in red, OVA-sVLNP is in green, and a merging of these photos indicates green elements approaching the nucleus. Figure 4B presents a quantitative analysis of the fluorescence intensity of OVA-sVLNP, which increased over time, indicating ongoing phagocytosis and processing of the nanoparticles by dendritic cells.

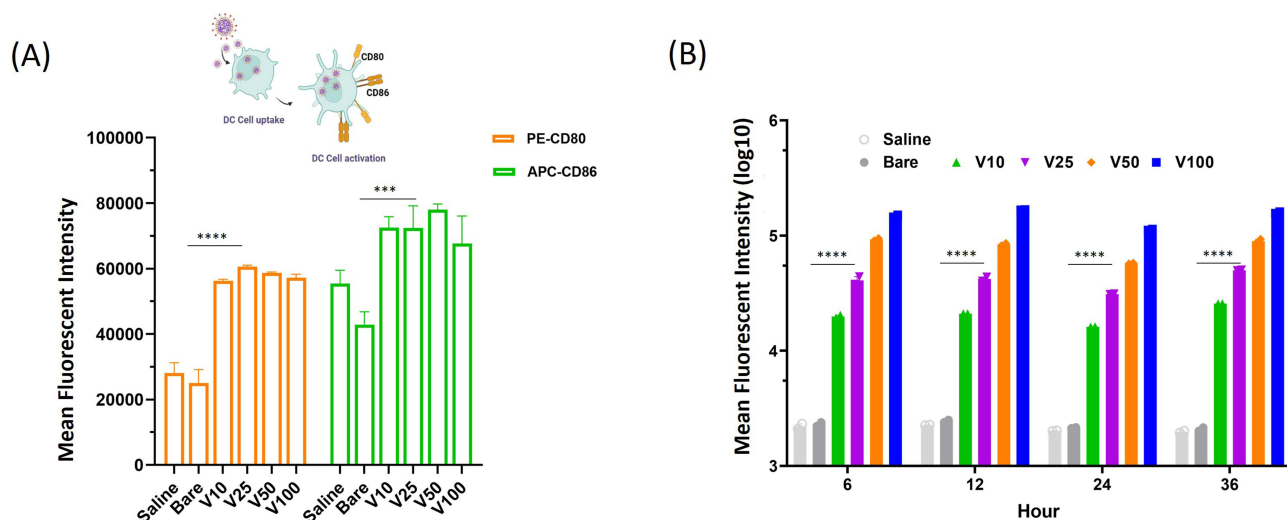


Figure 3 Flow cytometry analysis of the activation efficacy of OVA-sVLNP in dendritic cells. **(A)** The fluorescence intensity of CD80 and CD86 expression levels across OVA-sVLNP groups highlights significant differences, particularly between V25 and Bare ($n = 3$, $***p < 0.001$, $****p < 0.0001$). **(B)** Phagocytosis of OVA-sVLNP by dendritic cells was measured via the fluorescence intensity at 6, 12, 24, and 36 h with significant differences between the V25 and Bare groups ($n = 3$, $****p < 0.0001$). Saline: control group, Bare: nanoparticles without OVA, V10 ~ V100: varying concentrations of OVA-sVLNP.

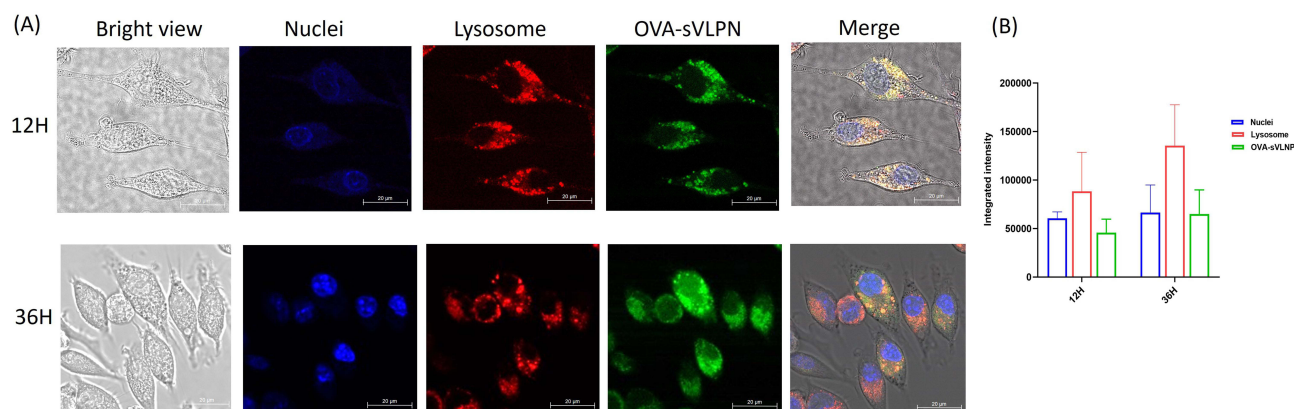


Figure 4 Phagocytosis evaluation of OVA-sVLNP in dendritic cells. **(A)** Confocal microscopy images displaying dendritic cells engulfing OVA-sVLNP. **(B)** Fluorescence quantification of each group at 12 and 36 h after OVA-sVLNP administration.

Biodistribution of OVA-sVLNP in Mice

In vivo imaging was utilized to track the biodistribution of OVA-sVLNP in vaccinated mouse models, as depicted in [Figure 5A](#). The mice received injections of OVA-sVLNP formulations (V10, V25, V50, and V100) into the muscle of the right hind leg. Fluorescent labeling of the nanoparticles enabled tracking of their location and quantification of accumulated fluorescence in the inguinal lymph nodes. XENOVEN Living Image 4.7 software was employed for this analysis with a focus on identifying the inguinal lymph nodes as the primary site of interest. The study observed that the OVA-sVLNP groups exhibited sustained accumulation at the injection site from 6 h to 72 h post-administration, as depicted in [Figure 5B](#). This prolonged retention at the injection site suggests an extended window for peripheral dendritic cell recruitment and enhanced opportunities for dendritic cell phagocytosis. Moreover, the OVA-sVLNP groups (V10, V25, V50, and V100) were found to reach the inguinal lymph nodes within 2 h post-administration, with sustained accumulation observed in these nodes for up to 7 days, as illustrated in [Figure 5C](#). Furthermore, [Figure 5C](#) reveals statistically significant differences ($*p < 0.05$, $**p < 0.01$, $***p < 0.001$, $****p < 0.0001$) in lymph node accumulation between the V25 and V100 groups at 6, 24, 48, 72 and 168 h. This prolonged residence time within the lymphatic system effectively extended antigen exposure, which is crucial for triggering an activated immune response in the mice. [Figure 1S](#) demonstrates the effective lymph node trafficking of the OVA-sVLNP groups (V10, V25, V50, and V100) at the 6-h mark, indicating successful delivery of OVA-sVLNP to the targeted lymph node locations.

Robust Humoral Immunity from Vaccinated Mouse Sera

In our mouse immunization model, a significant increase in IgG titers was observed across all groups following the initial administration of OVA-sVLNP, particularly on the thirty-fifth day. On this day, the mean IgG titers for the V10, V25, V50, and V100 groups were 13043 ng/mL, 392719 ng/mL, 105055 ng/mL, and 129351 ng/mL, respectively. The V25 group displayed significantly higher IgG titer than other groups ($****p < 0.0001$), indicating its superior immunogenicity. The IgG titers peaked or continued to rise on day 63 and remained high until the termination of the study on day 84. Notably, the V25 group maintained significantly elevated IgG titers compared with other groups ($*p < 0.05$). On day 63, the mean IgG titer for the V25 group was 334477 ng/mL, surpassing the mean IgG titers of the other groups: V10 (15612 ng/mL), V50 (176642 ng/mL), and V100 (175102 ng/mL), as depicted in [Figure 6A](#). [Figure 6C](#) illustrates the continuous distribution of IgG titers across all groups at various times, reinforcing the sustained and notably elevated immune response in the V25 group throughout the study duration.

Regarding IgG1 responses, the V25 group again demonstrated notably higher titers than all other groups. On day 35, the average IgG1 titer in the V25 group increased significantly to 188139 ng/mL, which was substantially higher than in the V10, V50, and V100 groups, which stood at 5034 ng/mL, 40116 ng/mL, and 49210 ng/mL, respectively ($****p < 0.0001$). The elevated IgG1 levels in the V25 group persisted through days 63 and 84. On day 63, the mean IgG1 titers were as follows: V25 (218334 ng/mL), V10 (10599 ng/mL), V50 (135987 ng/mL), and V100 (123739 ng/mL), with the V25 group

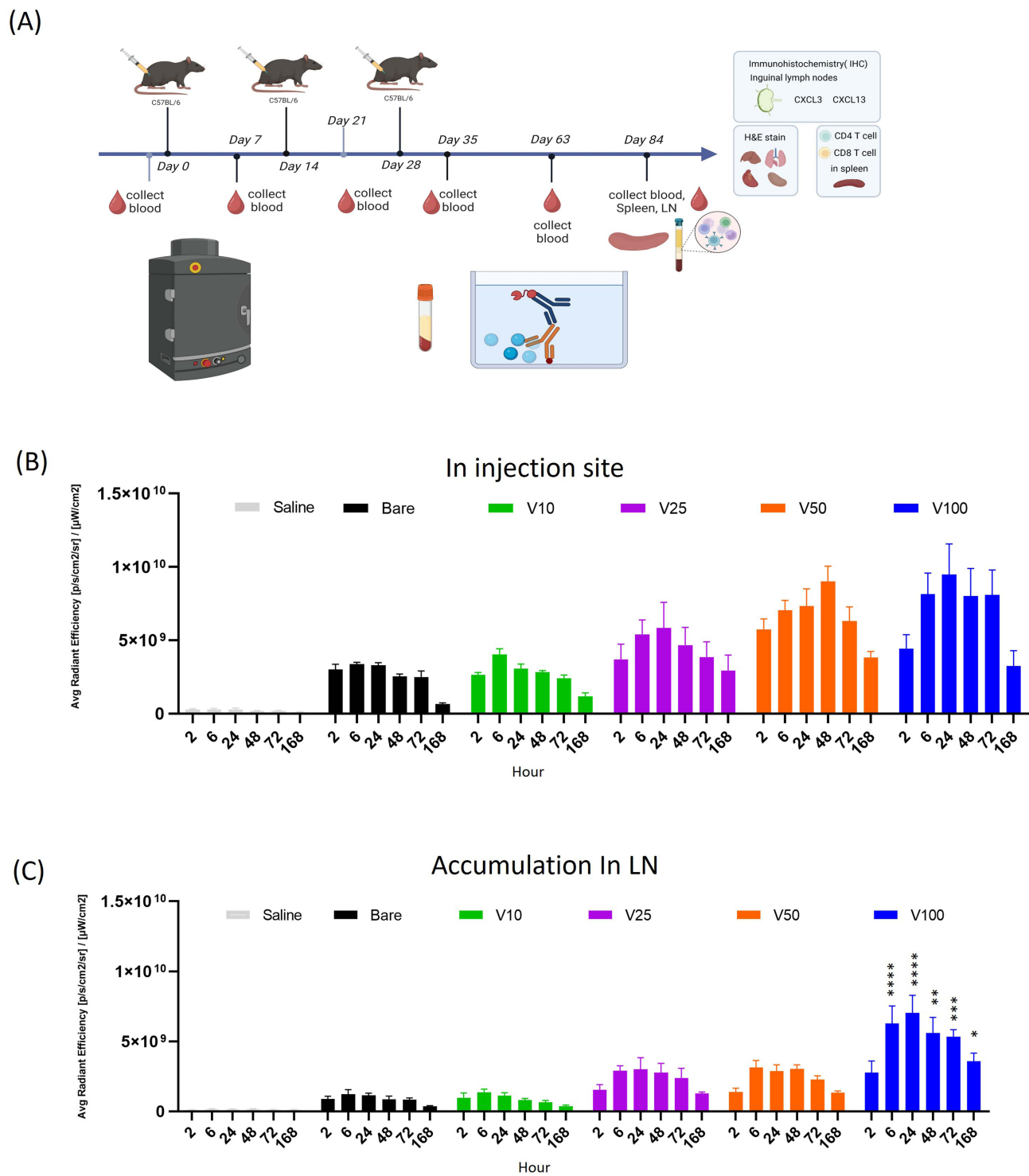


Figure 5 Biodistribution of OVA-sVLNP in mice. (A) Schematic diagram of vaccinated mouse models and evaluation methods. (B) Fluorescence intensity at the injection site was monitored over one week using an in vivo imaging system (n = 4). (C) Fluorescence intensity accumulation at lymph node sites was also monitored over one week, with significant differences between V25 and V100 at 6, 24, 48, 72, and 168 hours (*p < 0.05, **p < 0.01, ***p < 0.001, ****p < 0.0001).

retaining statistical significance from other groups (**p < 0.01), as depicted in Figure 6B. The IgG1 titers at various time points for each group are visually presented in Figure 6D.

Regarding the IgG2a titers, a distinct pattern emerged. The V10 exhibited a steep decline after day 21, whereas the other groups peaked at day 35 and then gradually diminished. Surprisingly, the V25 group did not manifest significantly

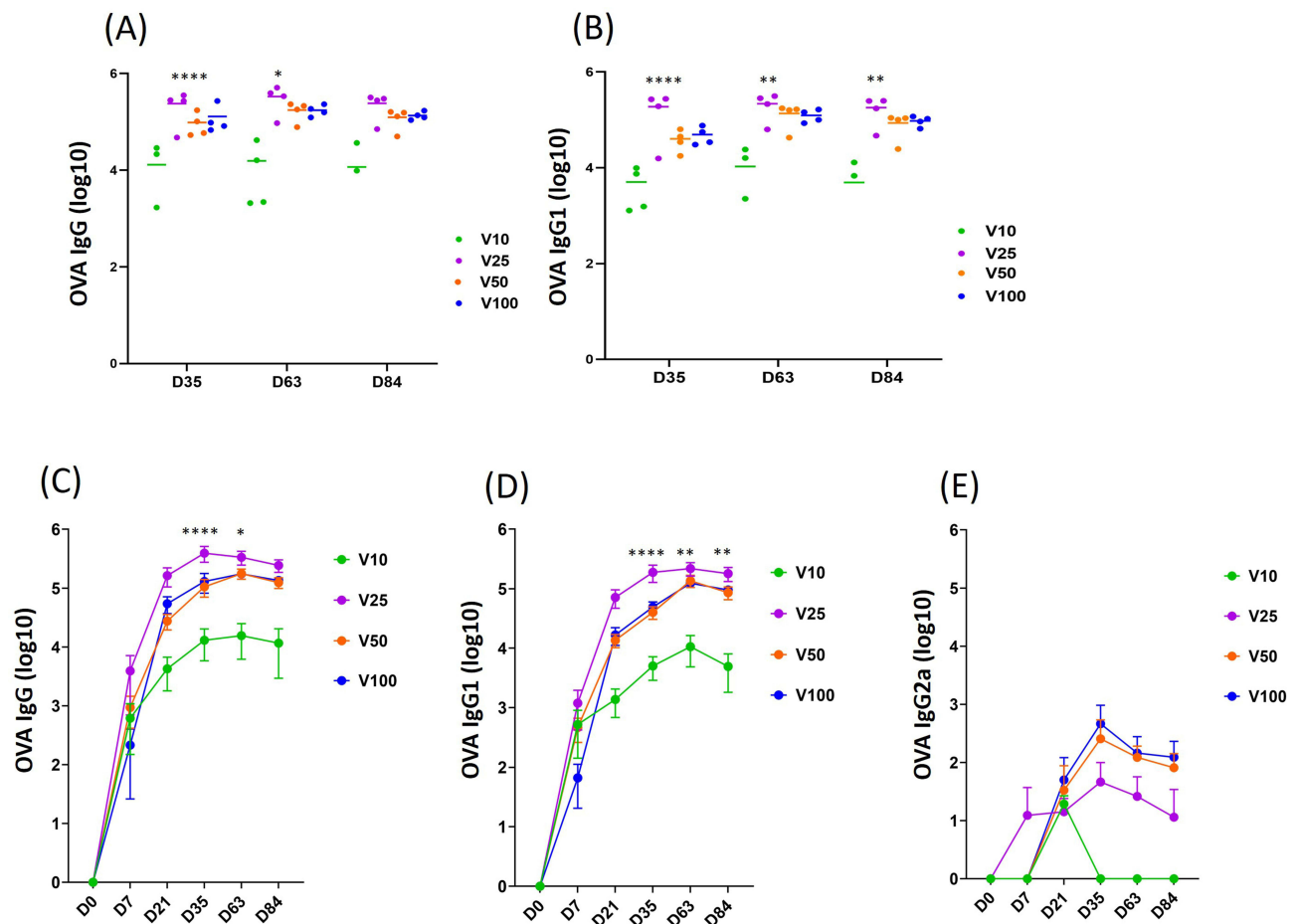


Figure 6 Humoral immunity responses in vaccinated mice. (A) Analysis of anti-ovalbumin immunoglobulin G (IgG) titers by ELISA up to 84 days post-administration. (B) Anti-ovalbumin immunoglobulin G1 (IgG1) titers were analyzed by ELISA up to 84 days post-administration. (C) The titer of IgG, (D) IgG1, and (E) IgG2a of mouse sera were determined and reported during the period, respectively ($n = 4$, * $p < 0.05$, ** $p < 0.01$, *** $p < 0.0001$).

higher IgG2a titers compared with the V50 and V100 groups, with no discernible differences observed, as illustrated in Figure 6E.

Splenocytes of Activated B Cells and T Cells in Mice

The study evaluated the activation ratios of B and T cells in murine spleens, which is critical for assessing the immune pathways induced by vaccination. Figure 7A illustrates that, compared with the control group, all OVA-sVLNP-treated groups exhibited an increase in B cells marked by CD45R⁺MHCII⁺ expression. Notably, the V25 group specifically stimulated a higher expression of CD45R⁺MHCII⁺ in B cells, reaching 61.8%. This group's elevated IgG titers and superior antibody protection underscore its effectiveness compared with other groups.

T cell profiling within the spleen was also conducted (Figure 7B and 7C), focusing on distinguishing CD3⁺ T cells into CD4⁺ (helper) and CD8⁺ (cytotoxic) subsets. CD3⁺CD4⁺ helper T cells constituted at least 54% of the OVA-sVLNP-affected T cell population, and CD3⁺CD8⁺ cytotoxic T cells represented over 33%. On day 84 after sVLNP administration, the OVA-sVLNP groups collectively manifested significantly increased proportions of CD4⁺ T cells compared with the control, albeit without discernible differences observed among the OVA-sVLNP groups. The V25 group displayed the highest percentage of CD3⁺CD4⁺CD8⁺ T cells at 5.96%, a significant increase compared with 1.8% in V10, 4.2% in V50, and 2.5% in V100. This finding aligns with previous studies that CD3⁺CD4⁺CD8⁺ T cells constitute mature effector memory lymphocytes, with specificity to antigens associated with latent and persistent viral infections (Figure 7D). Upon antigenic challenge in vivo, these double-positive cells exhibit superior functionality compared with single-positive cells, expressing cytokines pertinent to

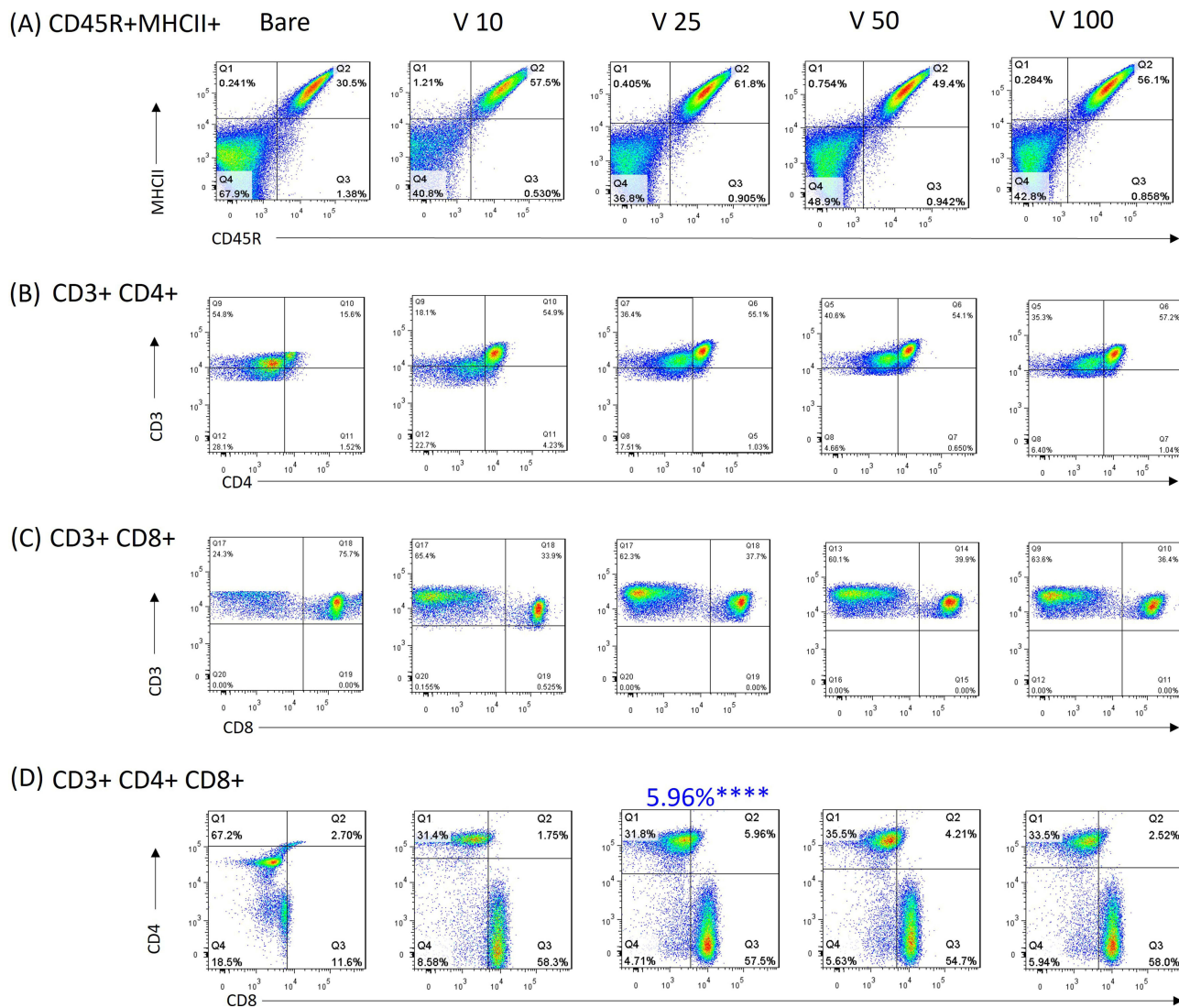


Figure 7 Activated percentage of B and T subset cells in mouse splenocytes. **(A)** Proportion of activated B cells marked by CD45R⁺MHCII⁺ expression. **(B)** Proportion of CD3⁺CD4⁺ T cells. **(C)** Proportion of CD3⁺CD8⁺ T cells. **(D)** Proportion of CD3⁺CD4⁺CD8⁺ T cells, with the V25 group demonstrating a prevalence of 5.96% (**** $p < 0.0001$).

helper and cytotoxic T cell functions and demonstrating heightened proliferation. These findings underscore their integral role in cellular immune responses, augmenting antiviral responses, and expanding the repertoire of immune-reactive T cell populations.

Multiple Cytokines Performance from Mouse Sera

Analysis of various cytokines in mouse serum revealed notable patterns in the V25 group, including cytokines such as IL-9, TNF- α , IL-2, IL-13, IL-10, IFN- γ , IL-4, IL-5, IL-17A, IL-17F, IL-22, and IL-6, as depicted in Figure 8. Specifically, a rapid increase in cytokine levels commenced on day 21 after the initial immunization, peaking on day 63. Remarkably, high levels of IL-9 and IL-10 in the V25 group were sustained until day 84, coinciding with the conclusion of the study. These multiple cytokine profiles exhibited significant differences in secretion compared with other groups on days 35, 63, and 84 ($*p < 0.05$, $**p < 0.01$, $***p < 0.001$, $****p < 0.0001$), signifying distinct immunomodulatory effects within the V25 group.

The Ratio of CXCL3 and CXCL13 in Mouse Lymph Nodes

Immunohistochemistry (IHC) staining of mouse lymph nodes revealed positive reactions for the chemokine CXCL-3 antibody across all experimental groups. Semiquantitative assessment with an established IHC color grading system revealed

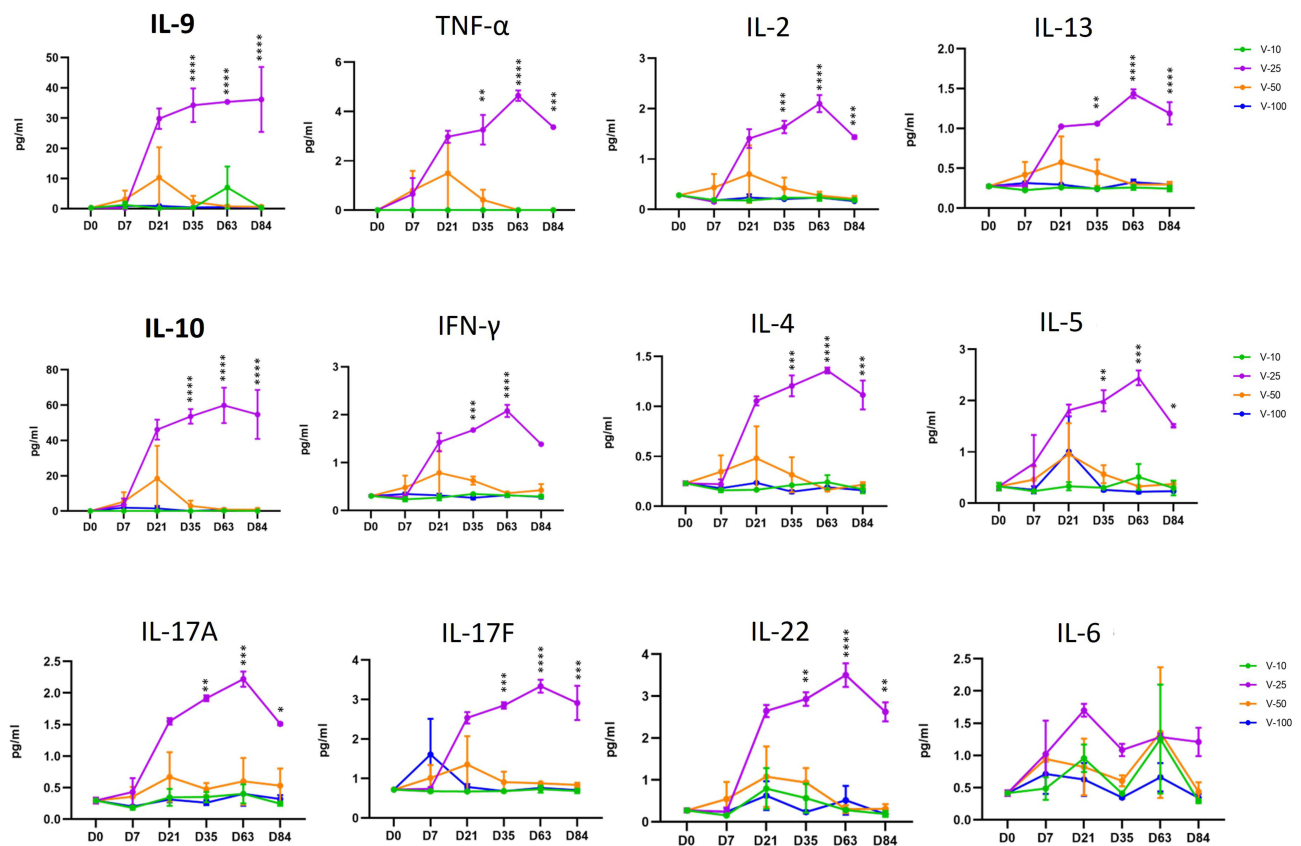


Figure 8 Cytokine responses from mouse sera in OVA-sVLNP groups. The data specifically highlight significant differences between V25 and other OVA-sVLNP groups. (n = 4, * $p < 0.05$, ** $p < 0.01$, *** $p < 0.001$, **** $p < 0.0001$).

that the V25 group exhibited the most intense staining (rating of 3+).³¹ Other groups, namely V10, displayed lower intensity (rating of 1+), whereas V50 and V100 exhibited intermediate staining (rating of 2+), as depicted in [Figure 9A](#) and [Table 4S](#).

By contrast, IHC staining for chemokine CXCL-13 exhibited negative outcomes for all experimental groups, implying an absence of detectable staining for chemokine CXCL-13 in the examined lymph nodes across the various treatment groups, as illustrated in [Figure 9B](#).

Biosafety Assessment

The H&E staining of tissue sections from each group revealed no noticeable abnormalities or signs of inflammatory reaction infiltration in the heart, liver, lung, and kidney tissues ([Figure 10A](#)). The enlarged H&E staining pictures (400X) of mouse lymph nodes from the OVA-sVLNP groups showed no immunotoxicity and no significant difference from the control groups ([Figure 2S](#)). Additionally, the body weight of mice across all groups remained consistent throughout the study ([Figure 10B](#)). These findings collectively indicate that the nanoparticle formulation under investigation has robust biological safety, with no apparent adverse effects on the examined organs or the overall physiological health of the experimental animals.

Discussion

The size profile of the synthesized OVA-sVLNP was crucial for enabling their efficient uptake by dendritic cells. This uptake played a key role in activating the dendritic cells and maintaining a sustained presence within the immune system, which in turn led to effective immune stimulation and the elicitation of a targeted immune response.

A key observation was the increased expression of CD80/86 cell surface markers on dendritic cells (DC) following the administration of OVA-sVLNP. This elevation strongly indicates effective DC activation in response to antigen stimulation. The enhanced expression of these costimulatory molecules signifies of a robust immune response initiated by

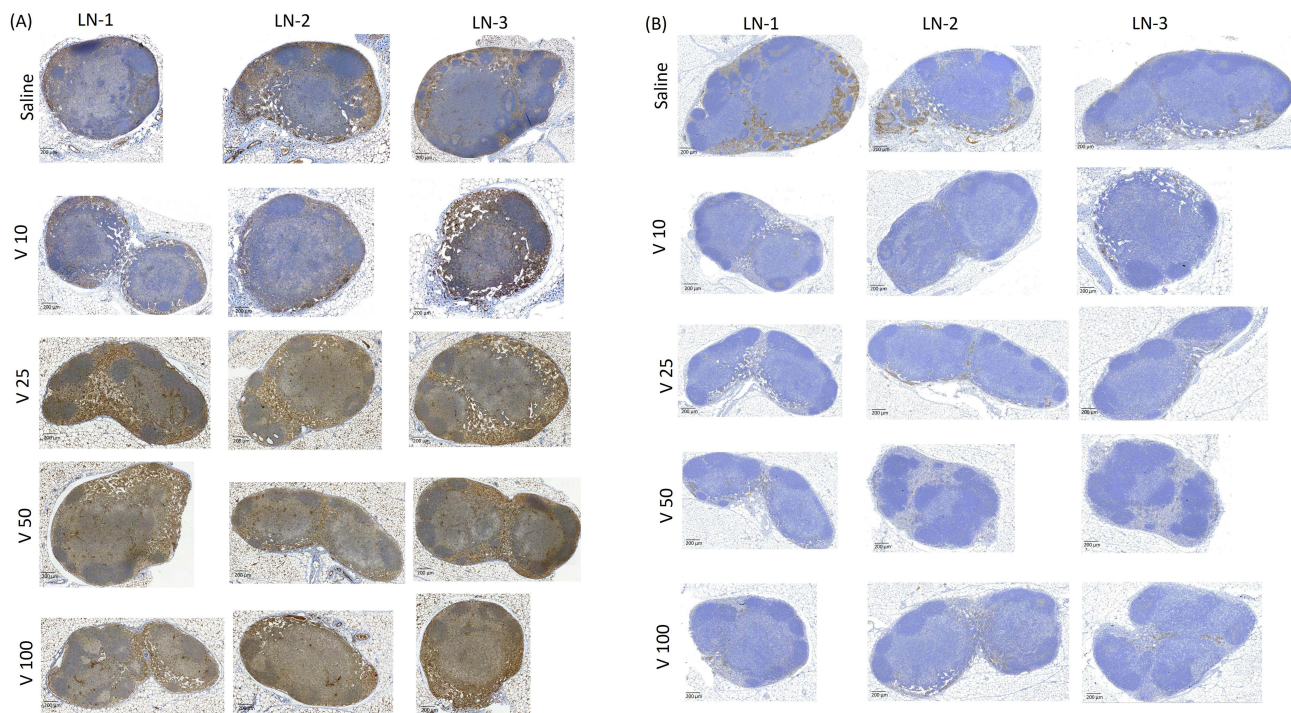


Figure 9 Chemokine distribution in mouse lymph nodes. **(A)** Immunohistochemistry (IHC) staining results for CXCL3 across experimental groups (scale bar: 200 μ m). **(B)** IHC staining results for CXCL13 across experimental groups (scale bar: 200 μ m).

OVA-sVLNP through dendritic cell activation.^{34,35} Furthermore, the intracellular processing of antigens within dendritic cells was observed, revealing the transit of OVA-sVLNP particles from the cytoplasm to the nucleus. This process, which includes passage through lysosomes before translocation to the nucleus, suggests a likely phagolysosome pathway. This insight is critical as it elucidates the antigen processing mechanism within dendritic cells and their potential impact on subsequent immune responses.

The repetitive protein fragment composition of OVA-sVLNP possesses a specific capacity to stimulate the immune system, thereby enhancing antigen presentation.³⁶ Notably, in the mouse models used in this study, the V25 group specifically exhibited a significant elevation in humoral immune responses, particularly in IgG and IgG1 antibodies, compared to other groups. This observation suggests that the effectiveness of the vaccine is not solely contingent on the administered dose. Instead, the resulting immune response to the drug appears intricately related to its dosage. The data indicate the optimal dosage range that maximizes immune response efficiency. Intriguingly, excessively high doses may lead to an overactive immune response, potentially resulting in immune exhaustion.³⁷ These findings are crucial for vaccine development, highlighting the necessity of determining the right dosage. Achieving an optimal balance in dosage is crucial to induce the desired immune response while avoiding unintended adverse effects such as immune exhaustion.

The assessment of cellular immunity, as determined through flow cytometry, revealed that OVA-sVLNP effectively induced the activation of T cells, including both CD3⁺CD4⁺ and CD3⁺CD8⁺T cells, within the spleens of the mouse model. A particularly noteworthy observation was the identification of a dual expression in the CD3⁺CD4⁺CD8⁺ cell population, indicating a unique cellular subset that exhibits characteristics of both helper and cytotoxic T cells. Moreover, the activation of B cells was evident through the upregulation of markers CD45R (B220) and MHC II within the spleen, signifying successful activation and training of B cells, which contributed to the generation of robust specific IgG antibodies. These observed cellular responses collectively demonstrate the effectiveness of OVA-sVLNP in eliciting a comprehensive immune activation involving both T and B cell compartments.

The analysis of various cytokines in the serum of mouse models, particularly focusing on the secretion levels of IL-9 and IL-10, revealed a distinct performance of the V25 group compared with other groups. The substantial secretion of IL-9 is intricately linked to the Th9 subset of T cells, a part of the broader classification of CD4⁺Th cells into Th1, Th2,

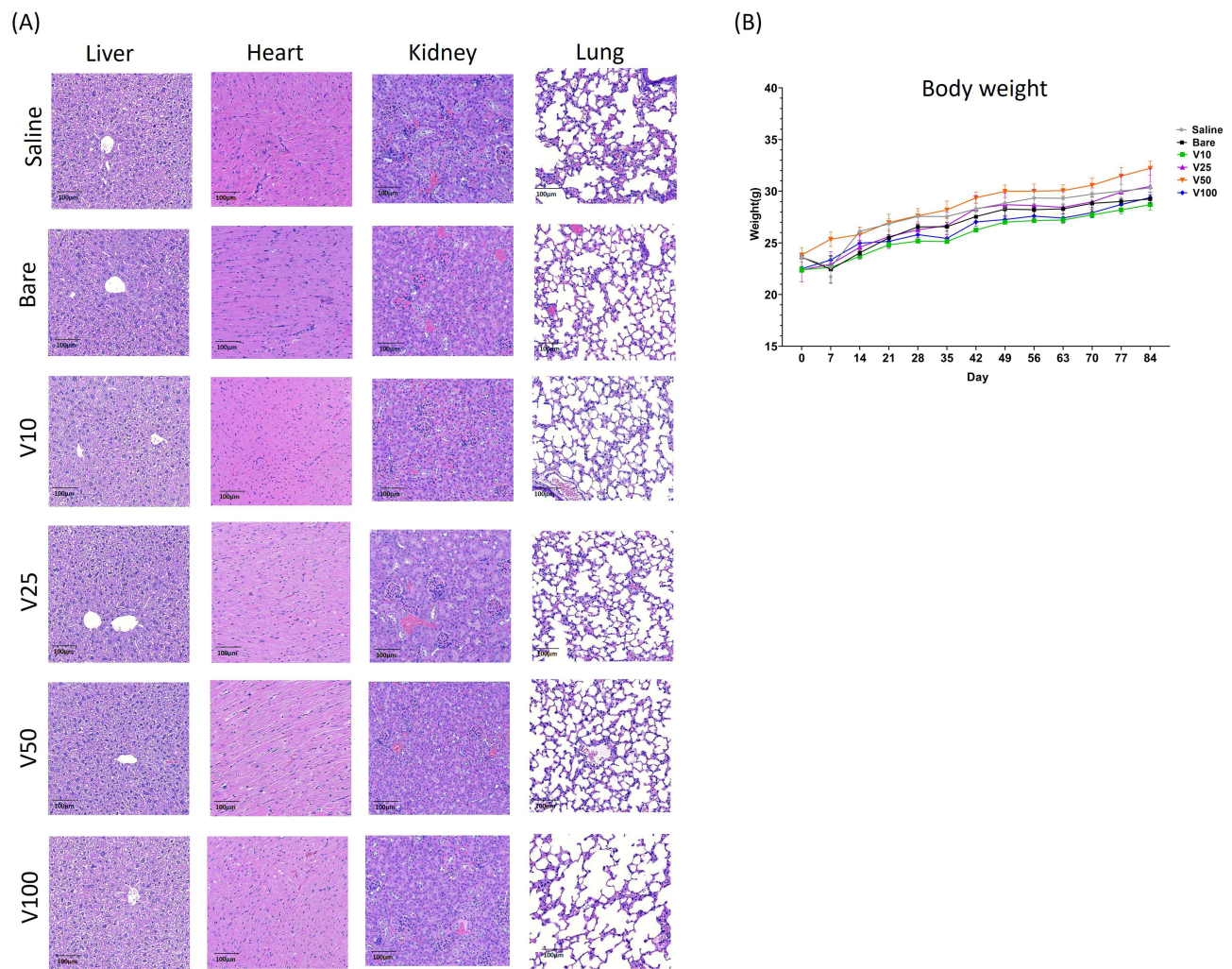


Figure 10 Biosafety assessment in mouse models. **(A)** H&E stained sections of hearts, livers, lungs, and kidneys. **(B)** Body weight monitoring of each experimental group over 84 days.

Th17, and Th9 subsets. Th9 cells, in particular, are closely associated with IL-9 secretion.³⁸ Therefore, we infer that the antitumor efficacy of OVA-sVLNP may be linked to Th9, given the increased secretion of IL-9.^{39,40} Moreover, the capacity of effector T cells in the solid tumor microenvironment to resist malignancies is correlated with the increase of IL-10, preventing tumor cells from inhibiting T cells within the tumor microenvironment. IL-10 enhances the ability of effector T cells to combat tumors.⁴¹ Notably, IL-10 secretion is not exclusive to regulatory T cells, as cytotoxic type 1 T cells (Tc1) also produce IL-10.⁴² This multifaceted role of IL-10 underscores its importance as an immunomodulator, potentially regulating immune responses and contributing to antitumor activities.

The immune response triggered by OVA-sVLNP reveals a complex interplay among various T cell subsets. The secretion of IL-10, extending beyond regulatory T cells to cytotoxic T cells (Tc1), enhancing their tumor-killing capabilities. Notably, IL-9 secreted by Th9 cells activates cytotoxic Tc9 cells,⁴² indicating potential plasticity as Tc9 cells can convert into Tc1 cells. This dynamic orchestration of immune responses involves a network of T cell subsets, emphasizing the intricate and multifaceted nature of OVA-sVLNP-induced responses. The surge in IL-9 and IL-10 levels underscores the comprehensive activation of diverse T cell pathways, contributing collectively to antitumor effects. Additionally, distinct cytokine secretion profiles in the V25 group, particularly TNF- α , IFN- γ , IL-2, IL-4, IL-5, IL-13, IL-17A, IL-17F, and IL-22, indicate a highly tailored immune response. TNF- α and IFN- γ play pivotal roles in aiding CD4⁺T cells against tumors,³⁸ and IL-2 enhances CD8⁺T cell and NK cell activity.³⁸

The secretion of IL-17 and IL-22, predominately associated with Tc17 cells, is influenced by the promotion of Th9 cells. This interplay stimulates various cytotoxic T cell subsets, including Tc9, Tc17, and Tc9-transformed Tc1 cells, setting the stage for a comprehensive and coordinated immune response aimed at combating tumor cells and the complex tumor microenvironment. The observed secretion of IL-4, IL-5, and IL-13, typically associated with Th2 responses, suggests their involvement in the immune reaction induced by OVA-sVLNP. Notably, Th9 cell differentiation is closely related to Th2 cells, suggesting that OVA-sVLNP might primarily activates Th9 cells in its antitumor mechanism.¹⁸ This inference is further supported by the notion that Th9 cells possess unique functions and responses compared with other Th subsets, making them particularly relevant in tumor immunity.³⁹ This distinctive immunological strategy, leveraging Th9 as the primary effector, offers promising potential for targeted therapeutic approaches in antitumor immunity.

The prominent IHC scoring for chemokine CXCL3, particularly in the V25 group, along with the notable accumulation of OVA-sVLNP in lymph nodes as depicted in Figure 5C, strongly suggests intensive T cell training within the lymph nodes of the mouse model. This observation aligns with the theoretical consensus that the induction of cellular immunity typically occurs subsequent to initial exposure. Hence, a robust and sustained cellular immune response is anticipated following the 3-month vaccination period. Additionally, the uniformly negative results in IHC for CXCL13, a chemokine associated with B cell training, provide intriguing insights. Given that the humoral immune response typically peaks around the 35th day following OVA protein injection, the IHC data collected on day 84 suggests that B cells within the lymphatic system have already completed their training earlier. Therefore, the role of CXCL13 in aiding B cell training might have been fulfilled earlier, leading to its reduced accumulation and distribution in mouse lymph nodes at later stages. This interpretation highlights the dynamic and temporally regulated orchestration of immune responses in the context of OVA-sVLNP vaccination.

While Figure 5C reveals greater lymph node accumulation for V100 in comparison to V25, the overall findings suggest that the V25 dosage stimulates and activates the immune system more substantially. The conclusion is drawn from the comprehensive evaluation of immune responses observed in the V25 group. The administration of excessively high antigen dose may disrupt immune system homeostasis and undermine its original functionality. Several explanations for this observation can be given. Firstly, immune cell anergy,⁴³ often observed in acute or chronic pathogen infections, may impair the activation of CD4⁺ cells, leading to reduced production of IgG antibodies by B cells. Secondly, high antigen doses could lead to saturation of the B cell receptor (BCR),⁴⁴ interfering with normal immune processes and potentially inducing immune tolerance, which may explain the lower antibody titers observed in the V50 and V100 groups. Finally, maintaining the balance between insufficient and excessive antigen presentation is critical. Insufficient presentation may hinder proper immune response, whereas excessive presentation may trigger a cytokine storm,⁴⁵ disrupting the immune balance. Therefore, determining the most appropriate antigen dose is pivotal for achieving optimal and balanced immune stimulation.

Conclusions

This study demonstrates the robust immunogenicity of OVA-sVLNP, as evidenced by the successful induction of potent, specific IgG antibodies and the stimulation of cellular immune responses, particularly the activation of tumor-killing Th9 cells. Utilizing a novel ELISA kit capable of simultaneously assessing of 12 immunological parameters, we observed a prevalent up-regulatory trend. Overall, the preliminary evidence not only enhances our understanding but also opens new avenues for advancements in cancer prevention, cell therapeutic techniques, and vaccine formulation. Additionally, the simplicity and cost-effectiveness of OVA-sVLNP manufacturing process offers promising directions for future research, potentially facilitating broader application and development.

Ethical Approval

All the animal experiments in this study were reviewed and approved by the Institutional Animal Care and Use Committee of Taipei Medical University (approval number LAC2022-0243) and in compliance with National Research Council's Guide for the Care and Use of Laboratory Animal.

Acknowledgments

Graphic Abstract and Illustrations were created with BioRender.com. This work was financially supported by the Ministry of Science and Technology, Taiwan (MOST 110-2314-B-038-041-MY3), the National Science and Technology Council, Taiwan (NSTC111-2622-8-038-007 PBF), and Taipei Medical University Hospital, Taipei, Taiwan (W0211).

Disclosure

The authors declare no conflicts of interest.

References

1. Coley WB. The treatment of inoperable sarcoma with the mixed toxins of erysipelas and bacillus prodigiosus. *JAMA*. 1989;XXXI.
2. Ruzzi F, Semprini MS, Scalambra L, et al. Virus-like Particle (VLP) Vaccines for Cancer Immunotherapy. *Int J Mol Sci*. 2023;24(16). doi:10.3390/ijms241612963
3. Janes ME, Gottlieb AP, Park KS, Zhao Z, Mitragotri S. Cancer vaccines in the clinic. *Bioeng. Transl. Med*. 2023. doi:10.1002/btm2.10588
4. Zhenyu Duan QL, Dai X, Xiaoling L, et al. Synergistic Therapy of a Naturally Inspired Glycopolymer-Based Biomimetic Nanomedicine Harnessing Tumor Genomic Instability. *Adv Mater*. 2021;33.
5. Lei Luob YQ, Zhongb H, Jiangb S, et al. GSH-sensitive polymeric prodrug: synthesis and loading with photosensitizers as nanoscale chemo-photodynamic anti-cancer nanomedicine. *Acta Pharmaceutica Sinica B*. 2022;12(1):424–436.
6. Haonan Li QG, Luo K. Biomarker-driven molecular imaging probes in radiotherapy. *Theranostics*. 2024;14(10):4127–4145.
7. Ru Wen ACU, Kou Y, Jian X. Ammad Ahmad Farooq. nanoparticle-systems-for-cancer-vaccine. *Nanomedicine*. 2019;14(5):627–648.
8. Mohsen DES MO, Knuth A, Bachmann MF. Virus-like particles for vaccination against cancer. *WIREs Nanomedi Nanobiotech*. 2019;e1579.
9. Liu X, Liu Y, Yang X, et al. Potentiating the Immune Responses of HBsAg-VLP Vaccine Using a Polyphosphoester-Based Cationic Polymer Adjuvant. *ACS Appl Mater Interfaces*. 2023;15(42):48871–48881. doi:10.1021/acsami.3c07491
10. Sander AF, Lollini PL. Virus-like antigen display for cancer vaccine development, what is the potential? *Expert Rev Vaccines*. 2018;17(4):285–288. doi:10.1080/14760584.2018.1455505
11. Palladini A, Thrane S, Janitzek CM, et al. Virus-like particle display of HER2 induces potent anti-cancer responses. *Oncoimmunology*. 2018;7(3):e1408749. doi:10.1080/2162402X.2017.1408749
12. Ong HK, Tan WS, Ho KL. Virus like particles as a platform for cancer vaccine development. *PeerJ*. 2017;5:e4053. doi:10.7717/peerj.4053
13. Tornesello AL, Tagliamonte M, Buonaguro FM, Tornesello ML, Buonaguro L. Virus-like Particles as Preventive and Therapeutic Cancer Vaccines. *Vaccines*. 2022;10(2). doi:10.3390/vaccines10020227
14. Bachmann MF, Jennings GT. Vaccine delivery: a matter of size, geometry, kinetics and molecular patterns. *Nat Rev Immunol*. 2010;10(11):787–796. doi:10.1038/nri2868
15. Plummer EM, Manchester M. Viral nanoparticles and virus-like particles: platforms for contemporary vaccine design. *Wiley Interdiscip Rev Nanomed Nanobiotech*. 2011;3(2):174–196. doi:10.1002/wnan.119
16. RA FC. Cell fate decision T-helper 1 and 2 subsets in immune responses. *Arthritis Res*. 2000;2:179–188.
17. Soroosh P, Doherty TA. Th9 and allergic disease. *Immunology*. 2009;127(4):450–458. doi:10.1111/j.1365-2567.2009.03114.x
18. Lu Y, Hong S, Li H, et al. Th9 cells promote antitumor immune responses in vivo. *J Clin Invest*. 2012;122(11):4160–4171. doi:10.1172/JCI65459
19. Noelle RJ, Nowak EC. Cellular sources and immune functions of interleukin-9. *Nat Rev Immunol*. 2010;10(10):683–687. doi:10.1038/nri2848
20. Kaplan MH, Hufford MM, Olson MR. The development and in vivo function of T helper 9 cells. *Nat Rev Immunol*. 2015;15(5):295–307. doi:10.1038/nri3824
21. Wan J, Wu Y, Ji X, et al. IL-9 and IL-9-producing cells in tumor immunity. *Cell Commun Signal*. 2020;18(1):50. doi:10.1186/s12964-020-00538-5
22. Xu J, Lv J, Zhuang Q, et al. A general strategy towards personalized nanovaccines based on fluoropolymers for post-surgical cancer immunotherapy. *Nat Nanotechnol*. 2020;15(12):1043–1052. doi:10.1038/s41565-020-00781-4
23. Toyota H, Yanase N, Yoshimoto T, Harada M, Kato Y, Mizuguchi J. Vaccination with OVA-bound nanoparticles encapsulating IL-7 inhibits the growth of OVA-expressing E.G7 tumor cells in vivo. *Oncol Rep*. 2015;33(1):292–296. doi:10.3892/or.2014.3603
24. Hou Y, Tang Z, Farheen J, et al. Ovalbumin-loaded paramagnetic nano-triangles for enhanced dendritic cell stimulation, T1-MR imaging, and antitumor immunity. *J Mater Sci Technol*. 2023;148:123–137. doi:10.1016/j.jmst.2022.11.024
25. Lu ZD, Chen YF, Shen S, Xu CF, Wang J. Co-delivery of Phagocytosis Checkpoint Silencer and Stimulator of Interferon Genes Agonist for Synergistic Cancer Immunotherapy. *ACS Appl Mater Interfaces*. 2021;13(25):29424–29438. doi:10.1021/acsami.1c08329
26. Danhier F, Ansorena E, Silva JM, Coco R, Le Breton A, Preat V. PLGA-based nanoparticles: an overview of biomedical applications. *J Control Release*. 2012;161(2):505–522. doi:10.1016/j.jconrel.2012.01.043
27. Michel Vert J. Biodegradation of PLA GA polymers: increasing complexity. *Biomaterials*. 1994;15:1209–1213.
28. Koerner J, Horvath D, Groettrup M. Harnessing Dendritic Cells for Poly (D,L-lactide-co-glycolide) Microspheres (PLGA MS)-Mediated Anti-tumor Therapy. *Front Immunol*. 2019;10:707. doi:10.3389/fimmu.2019.00707
29. Koerner J, Horvath D, Herrmann VL, et al. PLGA-particle vaccine carrying TLR3/RIG-I ligand Riboxim synergizes with immune checkpoint blockade for effective anti-cancer immunotherapy. *Nat Commun*. 2021;12(1):2935. doi:10.1038/s41467-021-23244-3
30. Martinez-Jothar L, Doukeridou S, Schifferers RM, et al. Insights into maleimide-thiol conjugation chemistry: conditions for efficient surface functionalization of nanoparticles for receptor targeting. *J Control Release*. 2018;282:101–109. doi:10.1016/j.jconrel.2018.03.002
31. McDonald JW, Pilgram TK. Nuclear expression of p53, p21 and cyclin D1 is increased in bronchioloalveolar carcinoma. *Histopathology*. 1999;34(5):439–446. doi:10.1046/j.1365-2559.1999.00632.x
32. Shnoudeh AJ, Hamad I, Abdo RW, et al. Synthesis, Characterization, and Applications of Metal Nanoparticles. *Bioma Bionanotech*. 2019;527–612. doi:10.1016/B978-0-12-814427-5.00015-9.

33. Lim TS, Goh JK, Mortellaro A, Lim CT, Hammerling GJ, Ricciardi-Castagnoli P. CD80 and CD86 differentially regulate mechanical interactions of T-cells with antigen-presenting dendritic cells and B-cells. *PLoS One*. 2012;7(9):e45185. doi:10.1371/journal.pone.0045185
34. Xiao Q, Xia Y. Insights into dendritic cell maturation during infection with application of advanced imaging techniques. *Front Cell Infect Microbiol*. 2023;13:1140765. doi:10.3389/fcimb.2023.1140765
35. Swiecki M, Colonna M. The multifaceted biology of plasmacytoid dendritic cells. *Nat Rev Immunol*. 2015;15(8):471–485. doi:10.1038/nri3865
36. Mohsen MO, Gomes AC, Vogel M, Bachmann MF. Interaction of Viral Capsid-Derived Virus-Like Particles (VLPs) with the Innate Immune System. *Vaccines*. 2018;6(3). doi:10.3390/vaccines6030037
37. Alahdal M, Elkord E. Exhaustion and over-activation of immune cells in COVID-19: challenges and therapeutic opportunities. *Clin Immunol*. 2022;245:109177. doi:10.1016/j.clim.2022.109177
38. Speiser DE, Chijioke O, Schaeuble K, Munz C. CD4(+) T cells in cancer. *Nat Cancer*. 2023;4(3):317–329. doi:10.1038/s43018-023-00521-2
39. You FP, Zhang J, Cui T, et al. Th9 cells promote antitumor immunity via IL-9 and IL-21 and demonstrate atypical cytokine expression in breast cancer. *Int Immunopharmacol*. 2017;52:163–167. doi:10.1016/j.intimp.2017.08.031
40. Rivera Vargas T, Humblin E, Vegran F, Ghiringhelli F, Apetoh L. T(H)9 cells in anti-tumor immunity. *Semin Immunopathol*. 2017;39(1):39–46. doi:10.1007/s00281-016-0599-4
41. Zhao Y, Chen J, Andreatta M, et al. IL-10-expressing CAR T cells resist dysfunction and mediate durable clearance of solid tumors and metastases. *Nat Biotechnol*. 2024. doi:10.1038/s41587-023-02060-8
42. Koh CH, Lee S, Kwak M, Kim BS, Chung Y. CD8 T-cell subsets: heterogeneity, functions, and therapeutic potential. *Exp Mol Med*. 2023;55(11):2287–2299. doi:10.1038/s12276-023-01105-x
43. Kaminski H, Lemoine M, Pradeu T. Immunological exhaustion: how to make a disparate concept operational? *PLoS Pathog*. 2021;17(9):e1009892. doi:10.1371/journal.ppat.1009892
44. Prechl J. A generalized quantitative antibody homeostasis model: regulation of B-cell development by BCR saturation and novel insights into bone marrow function. *Clin Transl Immunology*. 2017;6(2):e130. doi:10.1038/cti.2016.89
45. Kim JS, Lee JY, Yang JW, et al. Immunopathogenesis and treatment of cytokine storm in COVID-19. Review. *Theranostics*. 2021;11(1):316–329. doi:10.7150/thno.49713

International Journal of Nanomedicine

Dovepress

Publish your work in this journal

The International Journal of Nanomedicine is an international, peer-reviewed journal focusing on the application of nanotechnology in diagnostics, therapeutics, and drug delivery systems throughout the biomedical field. This journal is indexed on PubMed Central, MedLine, CAS, SciSearch®, Current Contents®/Clinical Medicine, Journal Citation Reports/Science Edition, EMBase, Scopus and the Elsevier Bibliographic databases. The manuscript management system is completely online and includes a very quick and fair peer-review system, which is all easy to use. Visit <http://www.dovepress.com/testimonials.php> to read real quotes from published authors.

Submit your manuscript here: <https://www.dovepress.com/international-journal-of-nanomedicine-journal>